

A General Strategy for Stretchable Microwave Antenna Systems using Serpentine Mesh Layouts

Tammy Chang, Yuji Tanabe, Charles C. Wojcik, Alex C. Barksdale, Sage Doshay, Zhenya Dong, Hao Liu, Maoyi Zhang, Yuli Chen, Yewang Su, Thomas H. Lee, John S. Ho, and Jonathan A. Fan*

Wireless functionality is essential for the implementation of wearable systems, but its adaptation in stretchable electronic systems has had limited success. In this paper, the electromagnetic properties of stretchable serpentine mesh-based systems is studied, and this general strategy is used to produce high-performance stretchable microwave systems. Stretchable mechanics are enabled by converting solid metallic sections in conventional systems to sub-wavelength-scale serpentine meshes, followed by bonding to an elastomeric substrate. Compared to prior implementations of serpentine meshes in microwave systems, this conversion process is extended to arbitrary planar layouts, including those containing curvilinear shapes. A detailed theoretical analysis is also performed and a natural tradeoff is quantified between the stretching mechanics and microwave performance of these systems. To explore the translation of these concepts from theory to experiment, two types of stretchable microwave devices are fabricated and characterized: a stretchable far-field dipole antenna for communications and a stretchable midfield phased surface for the wireless powering of biomedical implanted devices.

and consumer home environments. In recent years, new materials science breakthroughs in stretchable conductive interconnects have led to demonstrations of a broad range of stretchable microwave systems, including wearable radio-frequency identification (RFID) tags and sensors,^[1–4] reconfigurable antennas,^[5–7] wireless epidermal electronics,^[8–10] and systems for wireless power transfer.^[11–14] For biomedical and skin-wearable applications in particular, it is essential for these systems to mimic the soft and stretchable mechanics of skin.

Two general strategies exist for translating microwave components, such as antennas, transmission lines, and impedance elements, from rigid to stretchable form factors. The first strategy is to construct stretchable devices using composite materials, such as silver/polymer inks,^[3,15] liquid metals,^[5,7,14] or conductive nanowire

networks.^[16] This composite approach offers limited microwave performance due to the conductivities of these materials, which are typically no greater than 10^4 S cm^{-1} . The second strategy is to pattern a standard, low-loss microwave material into lateral spring structures^[17] or serpentine-type geometries,^[13,18,19] and transfer print the structure to an elastomeric substrate.

1. Introduction

Mechanically stretchable microwave systems represent a new wave of technologies central to the Internet of Things and have applications in agricultural, industrial, biomedical,

T. Chang, Dr. Y. Tanabe, C. C. Wojcik, A. C. Barksdale, S. Doshay, Prof. T. H. Lee, Prof. J. A. Fan
Department of Electrical Engineering
Stanford University
Stanford, CA 94305, USA
E-mail: jonfan@stanford.edu

Z. Dong, Prof. J. S. Ho
Department of Electrical and Computer Engineering
National University of Singapore
Singapore 117583, Singapore

H. Liu, M. Zhang, Prof. Y. Su
State Key Laboratory of Nonlinear Mechanics
Institute of Mechanics
Chinese Academy of Sciences
Beijing 100190, China

H. Liu, Y. Chen
Institute of Solid Mechanics
Beihang University (BUAA)
Beijing 100191, China

M. Zhang, Prof. Y. Su
School of Engineering Science
University of Chinese Academy of Sciences
Beijing 100049, China

Prof. Y. Su
State Key Laboratory of Structural Analysis for Industrial Equipment
Department of Engineering Mechanics
Dalian University of Technology
Dalian 116024, China

Prof. Y. Su
State Key Laboratory of Digital Manufacturing Equipment and Technology
Huazhong University of Science and Technology
Wuhan 430074, China

 The ORCID identification number(s) for the author(s) of this article can be found under <https://doi.org/10.1002/adfm.201703059>.

DOI: 10.1002/adfm.201703059

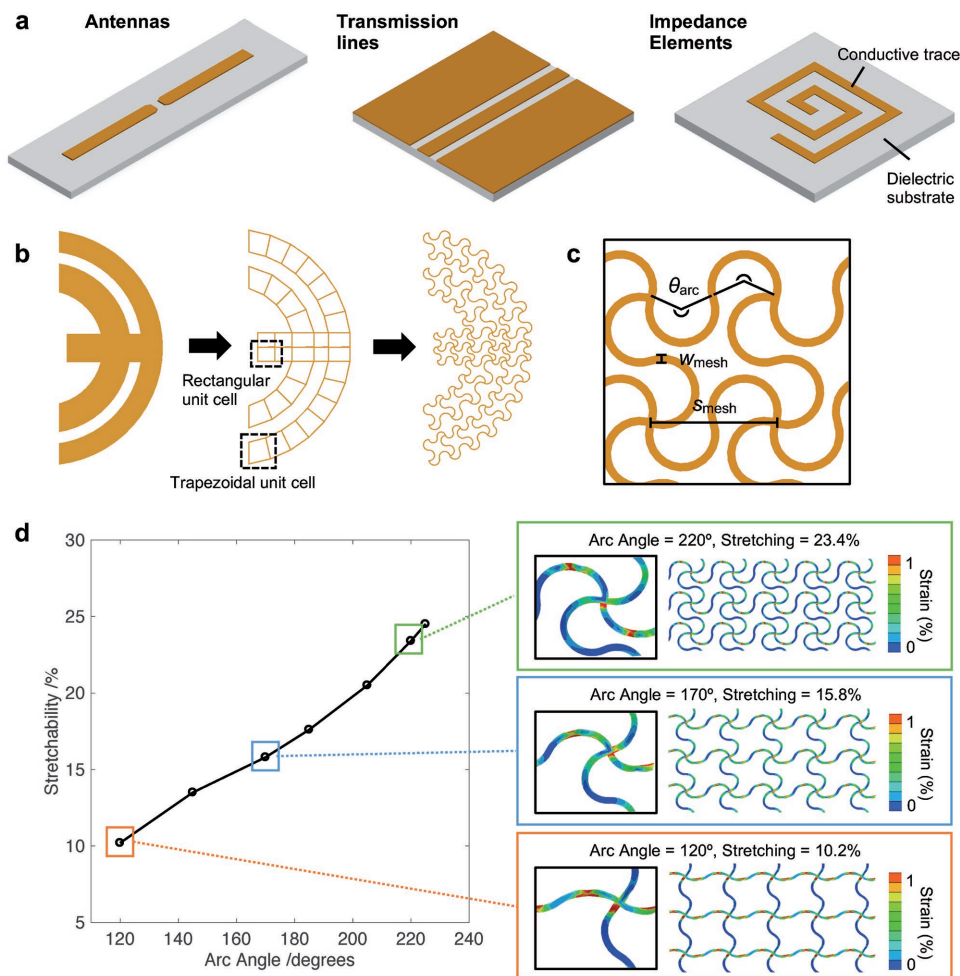


Figure 1. Stretchable microwave systems utilizing serpentine mesh layouts. a) Rigid planar microwave components on dielectric substrates. b) Conversion of a rigid metal section with a curvilinear layout to a mesh with rectangular and trapezoidal unit cells, then to a serpentine mesh layout. c) Detailed schematic of a square serpentine mesh unit cell described by its parameters arc angle θ_{arc} , mesh width w_{mesh} , and mesh spacing s_{mesh} . d) Mechanical simulations of serpentine mesh sections that have been uniaxially stretched until a maximum principal strain of 1% is measured along the wire cross section. Simulations are performed for serpentine meshes comprising seven different arc angle values. Strain along the mesh at maximum principal strain is shown for $\theta_{\text{arc}} = 120^\circ$, 170° , and 220° .

This approach is attractive because it offers the potential for high-performance microwave device operation, due to the high conductivity of conventional materials, such as copper laminates ($5.8 \times 10^5 \text{ S cm}^{-1}$). In addition, these devices can readily incorporate mechanically rigid electronic components onto lithographically defined bonding pads using conventional soldering methods.

In this paper, we analyze and implement a general strategy for converting rigid planar microwave systems to stretchable systems using serpentine mesh layouts (Figure 1a,b). Serpentine meshes have been previously studied as a general design tool for stretchable electronic and electromagnetic devices operating at DC or low frequencies.^[20,21] At these limits, the serpentine mesh period is orders of magnitude shorter than the operating wavelength, and the devices can be modeled in a straightforward fashion using electrostatic or quasistatic analyses. At higher microwave frequencies, however, complexities arise as the serpentine mesh period becomes a non-negligible fraction of the operating wavelength. In this case, the detailed

mesh layout can strongly impact the high-frequency impedance characteristics of these microwave components. These effects, and their impact on device performance, have not been studied in detail in prior work. In the first part of this study, we quantify the relationship between the detailed mesh geometry and its high-frequency impedance, and identify a proper design route to converting microwave devices from solid metal to mesh layouts. In the second part, we design and experimentally fabricate a stretchable far-field dipole antenna for communications and a mid-field phased surface designed for wireless power transfer. These demonstrations signify the applicability of our design methods to a broad range of planar microwave systems.

2. Conversion Strategy for Stretchable Serpentine Mesh Layouts

The conversion of a planar, solid metal microwave device from rigid to stretchable can be performed in an automated fashion

(Figure 1b). First, the metallic sections of the device are subdivided into a grid of subwavelength-scale unit cells, each with four sides, to form a mesh. For metallic sections that contain square or rectangular shapes, the unit cells naturally take the form of square or rectangular geometries. For metallic sections that contain curvilinear shapes, the unit cells can generalize to trapezoidal layouts, which can then be interconnected to describe regions of arbitrary curvature. Second, each of these unit cells is converted to a serpentine mesh by linking each adjacent vertex with two semicircles of equal arc angle θ_{arc} , which serve as lateral mechanical springs (Figure 1c).

As θ_{arc} increases, the metal trace connecting two adjacent vertices lengthens and the stretchability of the serpentine mesh increases. We quantify the relationship between mechanical stretching and arc angle using mechanical simulations. For this analysis, we simulate eight serpentine unit cells bounded by periodic boundary conditions. The mesh consists of 3 μm thick copper on 1 μm thick polyimide layers, and it is fully bonded onto a Solaris substrate (elastic modulus ≈ 60 kPa). Relatively thick copper is used to reduce power loss associated with electromagnetic skin-depth effects. The mesh widths and spacings are $w_{\text{mesh}} = 110$ μm and $s_{\text{mesh}} = 1.65$ mm, respectively. In the simulation, the periodic unit cells of serpentine geometries are stretched until the maximum principle strain of the metallic

serpentine cross section reaches 1% (Figure 1d). The stretchability of the serpentine clearly increases with increasing arc angle, as shown by the results for seven different simulated arc angles.

While previous investigations have systematically studied the relationship between mesh geometry and mechanical deformation,^[18,22] we extend this line of analysis and examine how changes to the serpentine mesh arc angle impacts microwave propagation. The conversion of metal sections from solid to serpentine and their mechanical stretching bring about impedance changes that directly affect microwave propagation. These impedance changes include modified resistances and inductances per unit length along the mesh layout, and they directly relate to changes in the curvature and morphology of the serpentine traces. We quantify the impact of these changes using the microstrip transmission line as a model system. We evaluate a microstrip section as it is converted from solid metal to a linear mesh with square unit cells, and then to serpentine meshes of arc angles ranging from 120° to 220° (Figure 2a). We also analyze the microstrip consisting of a 220° arc angle serpentine mesh, with and without stretching.

The simulated surface current distribution for several microstrip sections are shown in Figure 2b, where the current propagates from left to right. The current is concentrated in

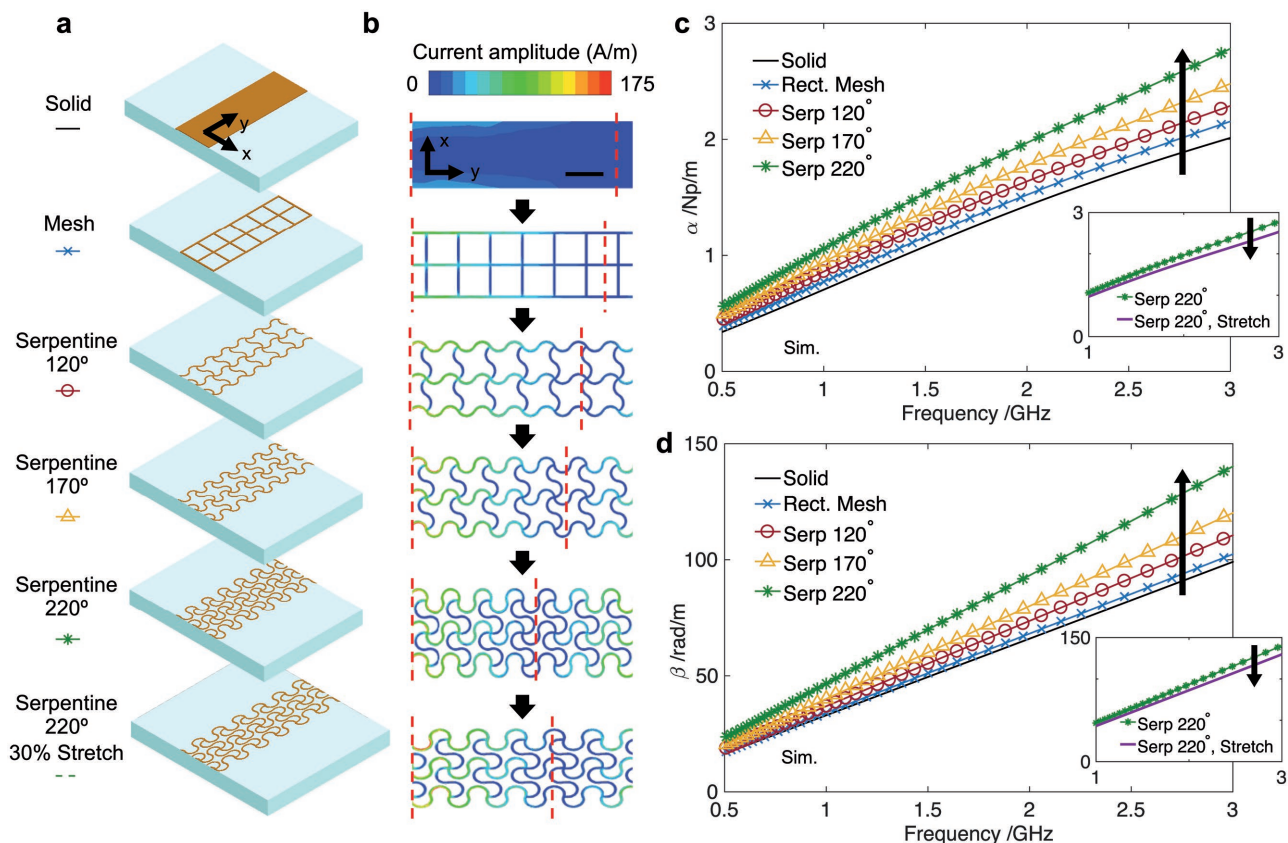


Figure 2. Analysis of a serpentine-based microstrip transmission line. a) Transmission line configurations utilizing solid, rectangular mesh, and serpentine mesh ($\theta_{\text{arc}} = 120^\circ, 170^\circ, 220^\circ$ unstretched, and 220° stretched). b) Simulated surface current distribution along each transmission line at 3 GHz. The current propagates in the positive y -direction, and the dotted red lines mark an effective electrical length of $\lambda/4$ for each layout. Scale bar: 2 mm. c, d) Attenuation constant α (c) and phase constant β (d) for each transmission line. Insets: Propagation constants of the serpentine-based transmission line ($\theta_{\text{arc}} = 220^\circ$) with and without 30% stretching.

the metal traces of the mesh that are oriented along the direction of propagation (i.e., the γ -direction, see Figure 2b for axes). As such, the overall physical length of these traces contributes directly to the effective electrical length of the transmission line. As noted earlier, the physical length of these traces increases as the mesh translates from a linear layout to a serpentine layout of increasing arc angle. Therefore, during this geometric conversion process, the effective electrical length increases and the effective wavelength decreases along the transmission line (see red lines, Figure 2b).

To further quantify this effect, we evaluate the complex electromagnetic propagation constant $\gamma = \alpha + j\beta$ for each transmission line. α is the attenuation constant in nepers per meter and contains information about propagation loss, while β is the phase constant in radians per meter and specifies the effective electrical length. To extract these propagation parameters from simulated transmission lines of finite length, we use a calibration method^[23] (also described in Figure S2, Supporting Information). We note that the characteristic impedance, Z_0 , is not available using this calibration method, and it will be further evaluated in future studies.

As the solid transmission line converts to a square mesh, and then to a serpentine mesh with increasing arc angle, the attenuation and phase constants both increase across the full range of simulated microwave frequencies (Figure 2c,d). At 2 GHz, α increases from 1.4 to 2 Np m⁻¹ and β increases from 65 to 92 rad m⁻¹ when it is converted from a solid metal trace to a serpentine mesh with $\theta_{\text{arc}} = 220^\circ$. The increase in α indicates that the microwave losses are higher along a serpentine transmission line compared to a solid transmission line. This increase in loss as the arc angle increases is attributed to the lengthening of traces for a given mesh vertex dimension, which yields larger overall resistance, as well as increased inductive coupling between adjacent traces. These observations point to an inherent tradeoff between mechanical stretchability and microwave power dissipation for serpentine microwave devices. To enhance mechanical stretching, the serpentine arc angle can be increased, at the expense of absorption losses. The increase in β after conversion, and subsequent reduction in effective wavelength, is consistent with our results in Figure 2b.

As the serpentine mesh is stretched, the effective wavelength of the propagating current increases. This effect is quantified in Figure 2d, where 30% stretching reduces β (or equivalently, increases the effective wavelength) by 7.6%, from 92 to 85 rad m⁻¹, at 2 GHz. There is also a 10% improvement in attenuation with stretching, from 2 to 1.8 Np m⁻¹ (Figure 2c). Physically, stretching unwinds the serpentine traces and decreases their arc angles, which reduces the inductive coupling between traces in the mesh and reduces propagation losses.

3. Fabrication and Analysis of Stretchable Microwave Antenna Systems

3.1. Serpentine Far-Field Dipole Antenna

Changes to effective wavelength and power attenuation observed for the microstrip transmission line upon stretching can be similarly expected for other metallic structures with similar

dimensions (relative to wavelength) when operated at microwave frequencies. For resonant antennas such as a far-field dipole antenna, the changes to effective wavelength can be observed by shifts in resonant frequency. Additionally, power attenuation along the antenna itself can be observed by differences in antenna gain and radiation efficiency. We note that the changes to effective wavelength and loss for these wire-based antennas will only be approximate to those observed with our microstrip transmission line study, due to their differing wave propagation mechanisms.

As a proof of concept, we analyze and fabricate a dipole antenna consisting of serpentine meshes with $w_{\text{mesh}} = 110 \mu\text{m}$, $s_{\text{mesh}} = 1.65 \text{ mm}$, and $\theta_{\text{arc}} = 220^\circ$. The antenna consists of 3 μm thick copper traces laminated with 1 μm thick polyimide and bonded to a Solaris substrate. Theoretical simulations show that the fundamental resonant frequency of the dipole antenna shifts as it converts from a solid to serpentine layout (Figure S3, Supporting Information). When the lengths of the serpentine and solid antennas are kept constant, this conversion produces a 19% decrease in resonant frequency, due to the increase in effective electrical length in the serpentine mesh (a phenomenon observed with the transmission line analysis). Based on these results, the overall length of dipole antennas should be reduced by approximately 19% compared to their solid equivalents, in order for the resonant frequency of the antenna to remain unaffected by the conversion process. We also observe that the radiation efficiency of the antenna decreases (Table S1, Supporting Information) as the antenna converts from solid to serpentine, indicating an increase in loss along the antenna. This result qualitatively agrees with the transmission line simulations, where attenuation increases as the solid metal waveguide converts to a serpentine mesh.

To characterize the antenna resonance as a function of stretching, we mount a fabricated dipole antenna on a balsa wood stand for mechanical stretching (Figure 3a). Details of the fabrication process are described in the Experimental Section and Figure S4. The measured return loss spectrum (Figure 3b) shows that the resonant frequency of the dipole decreases from 1.7 GHz to 1.37 GHz when the antenna's elastomer substrate is stretched from 0% to 30%, and correlates well with the simulated spectra (Figure 3c). To characterize the far-field radiation pattern of the serpentine dipole antenna, we measure our devices in stretched and unstretched configurations at resonance in an anechoic chamber (Figure 3d). The unstretched antenna resonates at 1.7 GHz, while the antenna uniaxially stretched to 20% resonates at 1.56 GHz. The far-field pattern (Figure 3e,f) does not change significantly with stretching, though we note an increase in antenna gain on the order of 0.5–1 dB when the device is stretched (Figure 3f). This increase in antenna gain is consistent with a reduction in loss as a function of increased stretching, which we observed in our transmission line analysis. This reduction in loss is also shown by the simulated radiation efficiency, which increases with stretching (Table S2, Supporting Information).

3.2. Serpentine Midfield Phased Surface

To show that our design concept can generalize to planar microwave devices of greater complexity, we analyze and fabricate a

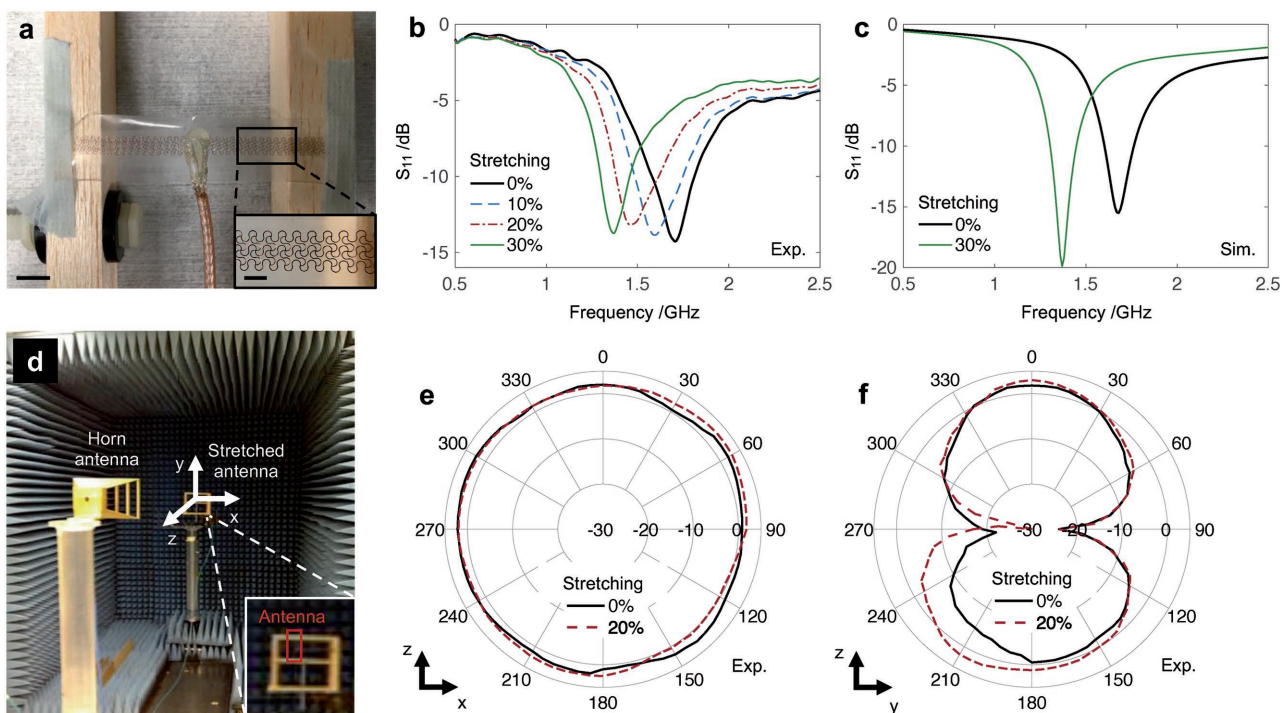


Figure 3. Experimental analysis of the serpentine dipole antenna. a) Fabricated dipole antenna mounted on a mechanical stretcher with the substrate stretched by 10%. Inset: detailed image of a section of the dipole antenna. Scale bars: 6 mm (main), 2 mm (inset). b) Return loss (S_{11}) spectra of the antenna uniaxially stretched at 0%, 10%, 20%, and 30%. c) Simulated return loss of the antenna uniaxially stretched at 0% and 30%. d) Image of the antenna mounted in the anechoic chamber for radiation pattern measurements. e, f) Radiation pattern measurements of the dipole antenna at 0% and 20% stretching. The patterns are measured at the corresponding dipole resonant frequency, which is 1.7 GHz for 0% stretching and 1.56 GHz for 20% stretching.

midfield phased surface consisting of concentric metal rings integrated with rigid passive components (Figure 4). This device has been demonstrated as a viable means for focusing microwave energy transfer into the human body, in order

to wirelessly power implanted biomedical devices.^[11,12,24,25] The device consists of concentric rings loaded with passive elements, which are used to engineer phases on the device surface. When the center port is excited with a continuous-wave

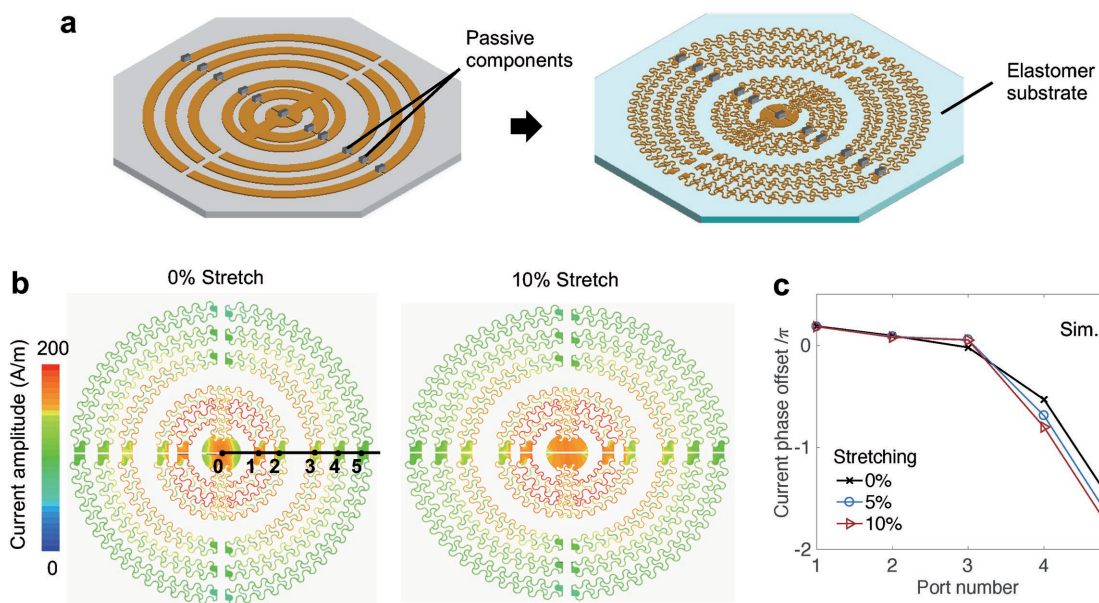


Figure 4. Serpentine midfield phased surface antenna. a) Schematic showing the conversion of a rigid microwave phased surface with passive components to its stretchable equivalent. b) Amplitude distribution (log scale) of surface current at 1.6 GHz for the phased surface under 0% and 10% stretching states. Ports 0–5 are labeled. c) Phase response of the lens, indicated by the phase offset between port 0 and port N for $N = 1$ to 5.

signal, oscillating currents are induced in the concentric rings. The radiation and interference of these currents produces the desired field pattern to focus energy to a target region within the body. While mechanically flexible versions of this phased surface have been demonstrated, a stretchable and soft system would allow full conformal contact to human skin and is useful for applications where the device must be worn for an extended period.

Our general strategy for converting solid metal structures into stretchable serpentine meshes extends to this system (Figure 4a). The solid metallic rings are translated into interlocking trapezoidal serpentine mesh unit cells, with $w_{\text{mesh}} = 300 \mu\text{m}$ and $\theta_{\text{arc}} = 175^\circ$. Compared with the dipole, a thicker trace width and decreased arc angle were selected for the phased surface to reduce microwave losses, which is important for power transfer applications. This improvement in device efficiency comes at the expense of mechanical stretchability. Solid metal pads are incorporated in the device pattern for the direct soldering of rigid reactive components to the device, which are used to specify the relative phases of the surface currents on each ring. Their values (0.1–1.2 pF; Table S3 and Figure S5, Supporting Information) were determined using

a numerical optimization scheme.^[12] To operate the phased surface at 1.6 GHz, the radius of the serpentine device was scaled down by 15% relative to the solid midfield antenna operating at 1.6 GHz, due to the increase in wavelength for the serpentine structure.

The serpentine phased surface is excited with a sinusoidal input wave and its surface current amplitude and phase are simulated with 0% and 10% stretching (Figure 4b,c) to verify that it is able to achieve the desired distributions required to focus microwave energy.^[11,12] The current amplitude at 1.6 GHz is larger in the center of the phased surface and drops off with a parabolic profile in the outer rings. Similarly, the phase response of the surface at 1.6 GHz also drops from approximately 0 to -2π from ports 1 to 5. These results demonstrate amplitude and phase profiles comparable to its solid counterpart and are not impacted by modest levels of stretching.^[12]

The device is fabricated (Figure 5a) using a similar process to the dipole antenna. The experimental setup shown in Figure 5b is used to test wireless powering performance in water, which mimics biological tissue, using a light-emitting micro-device to detect the intensity of the magnetic field generated

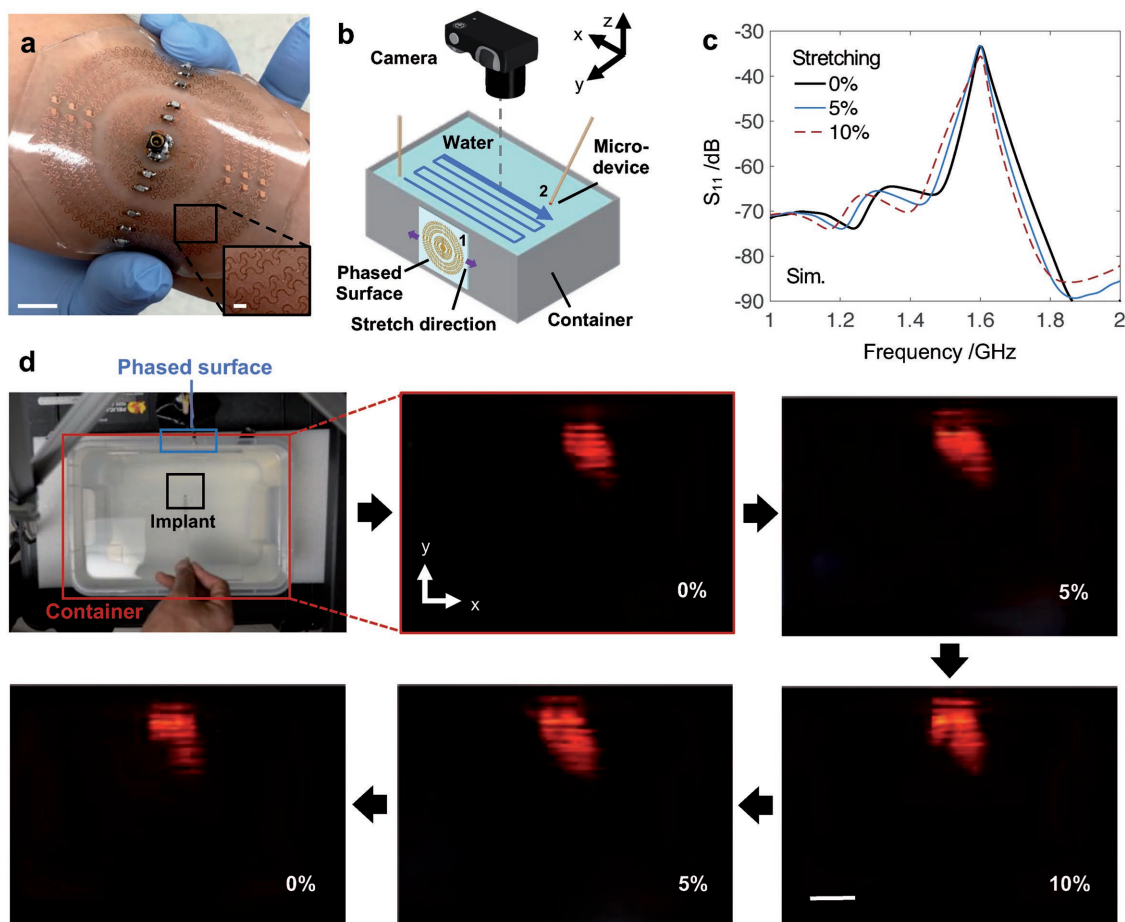


Figure 5. Experimental characterization of the serpentine midfield phased surface antenna. a) Fabricated serpentine phased surface. Scale bars: 6 mm (main figure), 2 mm (inset). b) Experimental setup for measuring wireless powering performance of the phased surface. Ports 1 and 2 are marked. c) Simulation of power transfer efficiency (S_{21}) with 0%, 5%, and 10% stretching between phased surface and microdevice implanted in deep tissue at 4.6 cm. d) Time-lapse images of light-emitting microdevice with stretching from 0% to 10%, then back to 0%. Scale bar: 4 mm.

by the serpentine surface (details in the Experimental Section; Figure S6, Supporting Information). The efficiency of power transfer from the phased surface to the microdevice, determined by the transmission scattering parameter S_{21} , is shown in Figure 5c. The microdevice is located at 4.6 cm from the surface in deep tissue. The power transfer efficiency at 1.6 GHz is -33.4 dB, which is comparable to values for a solid phased surface (-32.5 dB at a similar depth).^[11] It is also evident from that the efficiency does not change significantly with 10% stretching. There is a maximum decrease of 2.2 dB from -33.4 dB at 0% stretching to -35.6 dB at 10%. This decrease is attributed to a small shift in resonance at the phased surface upon stretching. We anticipate that at higher levels of stretching and no adjustment in input signal frequency, the efficiency would be reduced by a greater extent. Measurements of the beam profile are shown in the time-lapse images (Figure 5d) as the substrate is stretched from 0% to 10%, and then back to 0%. The light emission patterns reveal a focused region in which wireless powering is highly efficient, demonstrating the ability of the serpentine structure to shape the microwave field within the volume. The overall field pattern does not change considerably at these levels of stretching. These results confirm that for modest levels of stretching, relatively complex serpentine microwave devices can achieve comparable performance to their solid counterparts.

4. Conclusion

In summary, the findings presented in this paper provide a general methodology for the design of stretchable planar microwave devices, where metallic structures can be translated into stretchable serpentine meshes. We find there is a natural tradeoff between the stretching mechanics and microwave performance of systems based on serpentine mesh layouts, demonstrated by mechanical and electromagnetic simulation results. With this tradeoff in mind, we have designed and experimentally demonstrated a stretchable far-field dipole antenna and midfield phased surface, showing that our design concepts can generalize to a broad range of stretchable planar microwave systems.

5. Experimental Section

Finite Element Analysis: The serpentine mesh geometries were imported into the preprocessor in ABAQUS, a finite element program (Dassault-Systèmes, Abaqus Analysis User's Manual, v.6.10, Dassault Systèmes Simulia Corp., Rhode Island, 2010). The serpentine layouts consisting of both copper and polyimide layers were modeled by four-node composite shell elements, sharing nodes with the soft Solaris substrate, which was modeled by eight-node solid elements. An ideal elastic-plastic constitutive model was used for the copper layer. Uniaxial stretch along the horizontal direction was applied to the entire structure, as shown in Figure 1d and Figure S1 in the Supporting Information, and the distribution of maximum principle strain of the top surface was obtained with 1% as the cutting value. We noted that the element number may be immense for larger models with more unit cells. As such, the serpentine meshes were simulated with a periodic model, which was scalable for larger designs (Figure S1, Supporting Information).

Fabrication of Copper Serpentine Mesh on Silicone Substrates: Polyimide (PI) was spun-cast (6000 r.p.m. for 60 s) on copper foil (3 μm , copper carrier 35 μm , Olin Brass). A two-step curing process for the PI included an initial bake on a hotplate in air (100 $^{\circ}\text{C}$, 10 min) followed by baking in a low oxygen environment (230 $^{\circ}\text{C}$, 2 h). The PI side was then pressed onto a silicon wafer coated with PDMS (Sylgard 184 Elastomer, Dow Corning, 10:1 weight ratio, 6000 r.p.m. at 60 s). Photolithography (Microposit S1813) and etching (CE-100 copper etchant, Transene Company, at room temperature for ≈ 4 min) defined patterns in the copper layer. Oxygen plasma etching (100 mTorr, 2 sccm O_2 , 300 watts for 30 min) patterned the PI to match the geometry of the metal traces. Water-soluble tape (3M) retrieved the device from the wafer, and electron beam evaporation of Ti (5 nm)/ SiO_2 (50 nm) formed backside coatings to enhance adhesion of the copper to a receiving substrate. Thin silicone substrates (≈ 2 mm thick, PDMS or Solaris, Smooth-on) were cast (30:1 weight ratio for PDMS, 1:1 for Solaris). Air plasma treatment was applied to the surfaces of the cast silicone (35 W for 10 s) and SiO_2 (35 W for 60 s) bonding layer of the device, and the serpentine structures were transferred to the silicone surface with the SiO_2 layer facing down. The sample was then submerged in water for 1 h to dissolve and remove the water-soluble tape.

Fabrication of Serpentine Devices: After bonding of the copper serpentine mesh to a silicone substrate, a final coat of PDMS (30:1, 2000 r.p.m. at 60 s, baked on hotplate at 100 $^{\circ}\text{C}$ for 20 min) was used to coat the surface. For the dipole antenna, a coaxial feed (SMA-RG316, 50 Ω , Pasternack) is soldered to the exposed metal pads for each dipole arm. For the phased surface device, packaged capacitors (0805 surface-mount) and coaxial feeds (SMA-MMCX, 50 Ω , Amphenol) were soldered to the exposed metal pads at the center of the phased surface.

Electromagnetic Simulation: Transmission line and dipole antenna simulations were conducted with Ansys HFSS v17, and phased surface simulations were conducted with CST Microwave Studio. The substrate is PDMS (dielectric constant = 3, loss tangent = 0.014) is used as the substrate and metal is copper (conductivity = $5.8 \times 10^7 \text{ S m}^{-1}$) for all simulations. For transmission line simulations, the substrate thickness is 1.35 mm and the loss tangent is increased to 0.04 to improve computational accuracy. Additionally, the ground plane is solid for the transmission line simulations to simplify the analysis.

Phased Surface Power Transfer Measurements: The phased surface was mounted on the side of a plastic container (dimensions 17.5 \times 26 \times 10 cm) filled with water (side view in Figure S6, Supporting Information). An RF signal generator connected to a power amplifier provided energy to the phased surface through a coaxial cable and a connector (MMCX, 50 Ω). The input frequency and power at the input to the phased surface is 1.612 GHz and 39 dBm. Power was wirelessly transferred to a microdevice consisting of a helical coil (2 mm diameter, 2 mm length) mounted on a circuit board, containing a rectifying circuit and red light-emitting diode, and encapsulated in transparent silicone (Figure S6b,c, Supporting Information). A time-lapse image was taken while the receiving LED device was mounted on the tip of a nonmetallic rod and swept across the container longitudinally and laterally in the x- and y-directions.

Supporting Information

Supporting Information is available from the Wiley Online Library or from the author.

Acknowledgements

The fabrication in this work was completed in the Stanford Nanofabrication Facility, Stanford Nano Shared Facilities, and Stanford Applied Nanophotonics Laboratory. The authors would like to acknowledge Dan Gregoire and Calvin Yang for their assistance

in measurements and simulation relating to this work, as well as Thabao Phan, Lucia Gan, Nemat Dolatsha, Timothy McKenna, and Nicholas Saiz for contributing their discussion and feedback. T. Chang acknowledges the government support by the U.S. Department of Defense (DoD) Air Force Office of Scientific Research through the National Defense Science & Engineering Fellowship (NDSEG) Program, 32 CFR 168a. J. A. Fan acknowledges the support from the National Science Foundation (No. CMMI-1637446) and the Packard Fellowship Foundation. Y. Su acknowledges the support from NSFC (No. 11572323), the Chinese Academy of Sciences via the "Hundred Talent program," the strategic priority research program of the Chinese Academy of Sciences (No. XDB22040501), the State Key Laboratory of Structural Analysis for Industrial Equipment, Dalian University of Technology (No. GZ1603), the State Key Laboratory of Digital Manufacturing Equipment and Technology, and Huazhong University of Science and Technology (No. DMETKF2017008).

Conflict of Interest

The authors declare no conflict of interest.

Keywords

antennas, microwaves, serpentine meshes, stretchable electronics

Received: June 6, 2017

Revised: August 7, 2017

Published online: October 16, 2017

- [1] J. Jeon, H.-B.-R. Lee, Z. Bao, *Adv. Mater.* **2013**, *25*, 850.
- [2] B. Zhu, H. Wang, W. R. Leow, Y. Cai, X. J. Loh, M.-Y. Han, X. Chen, *Adv. Mater.* **2016**, *28*, 4250.
- [3] J. Suikkola, T. Björninen, M. Mosallaei, T. Kankkunen, P. Iso-Ketola, L. Ukkonen, J. Vanhala, M. Mäntysalo, *Sci. Rep.* **2016**, *6*, 25784.
- [4] S. Cheng, Z. Wu, *Adv. Funct. Mater.* **2011**, *21*, 2282.
- [5] M. Kubo, X. Li, C. Kim, M. Hashimoto, B. J. Wiley, D. Ham, G. M. Whitesides, *Adv. Mater.* **2010**, *22*, 2749.
- [6] Z. Wu, K. Hjort, S. H. Jeong, *Proc. IEEE* **2015**, *103*, 1211.
- [7] M. Zandvakili, M. M. Honari, D. Sameoto, P. Mousavi, *IEEE MTT-S Int. Microw. Symp.* **2016**.
- [8] D.-H. Kim, N. Lu, R. Ma, Y.-S. Kim, R.-H. Kim, S. Wang, J. Wu, S. M. Won, H. Tao, A. Islam, K. J. Yu, T. Kim, R. Chowdhury, M. Ying, L. Xu, M. Li, H.-J. Chung, H. Keum, M. McCormick, P. Liu, Y. Zhang, F. G. Omenetto, Y. Huang, T. Coleman, J. A. Rogers, *Science* **2011**, *333*, 838.
- [9] S. Xu, Y. Zhang, L. Jia, K. E. Mathewson, K.-I. Jang, J. Kim, H. Fu, X. Huang, P. Chava, R. Wang, S. Bhole, L. Wang, Y. J. Na, Y. Guan, M. Flavin, Z. Han, Y. Huang, J. A. Rogers, *Science* **2014**, *344*, 70.
- [10] H. Araki, J. Kim, S. Zhang, A. Banks, K. E. Crawford, X. Sheng, P. Gutruf, Y. Shi, R. M. Pielak, J. A. Rogers, *Adv. Funct. Mater.* **2016**, *27*, 1604465.
- [11] D. R. Agrawal, Y. Tanabe, D. Weng, A. Ma, S. Hsu, S.-Y. Liao, Z. Zhen, Z.-Y. Zhu, C. Sun, Z. Dong, F. Yang, H. F. Tse, A. S. Y. Poon, J. S. Ho, *Nat. Biomed. Eng.* **2017**, *1*, 1.
- [12] J. S. Ho, B. Qiu, Y. Tanabe, A. J. Yeh, S. Fan, A. S. Y. Poon, *Phys. Rev. B* **2015**, *91*, 1.
- [13] X. Huang, Y. Liu, G. W. Kong, J. H. Seo, Y. Ma, K.-I. Jang, J. A. Fan, S. Mao, Q. Chen, D. Li, H. Liu, C. Wang, D. Patnaik, L. Tian, G. A. Salvatore, X. Feng, Z. Ma, Y. Huang, J. A. Rogers, *Microsyst. Nanoeng.* **2016**, *2*, 16052.
- [14] S. H. Jeong, K. Hjort, Z. Wu, *Sci. Rep.* **2015**, *5*, 8419.
- [15] Z. Li, T. Le, Z. Wu, Y. Yao, L. Li, M. Tentzeris, K. S. Moon, C. P. Wong, *Adv. Funct. Mater.* **2015**, *25*, 464.
- [16] L. Song, A. C. Myers, J. J. Adams, Y. Zhu, *ACS Appl. Mater. Interfaces* **2014**, *6*, 4248.
- [17] A. M. Hussain, F. A. Ghaffar, S. I. Park, J. A. Rogers, A. Shamim, M. M. Hussain, *Adv. Funct. Mater.* **2015**, *25*, 6565.
- [18] Y. Su, X. Ping, K. J. Yu, J. W. Lee, J. A. Fan, B. Wang, M. Li, R. Li, D. V Harburg, Y. Huang, C. Yu, S. Mao, J. Shim, Q. Yang, P. Lee, A. Armonas, K. Choi, Y. Yang, U. Paik, T. Chang, T. J. Dawidczyk, Y. Huang, S. Wang, J. A. Rogers, *Adv. Mater.* **2017**, *29*, 160489.
- [19] Y. H. Jung, J. Lee, Y. Qiu, N. Cho, S. J. Cho, H. Zhang, S. Lee, T. J. Kim, S. Gong, Z. Ma, *Adv. Funct. Mater.* **2016**, *26*, 4635.
- [20] S. Han, M. K. Kim, B. Wang, D. S. Wie, S. Wang, C. H. Lee, *Adv. Mater.* **2016**, 10257.
- [21] Y. K. Lee, K.-I. Jang, Y. Ma, A. Koh, H. Chen, H. N. Jung, Y. Kim, J. W. Kwak, L. Wang, Y. Xue, Y. Yang, W. Tian, Y. Jiang, Y. Zhang, X. Feng, Y. Huang, J. A. Rogers, *Adv. Funct. Mater.* **2017**, *27*, 1605476.
- [22] J. A. Fan, W.-H. Yeo, Y. Su, Y. Hattori, W. Lee, S.-Y. Jung, Y. Zhang, Z. Liu, H. Cheng, L. Falgout, M. Bajema, T. Coleman, D. Gregoire, R. J. Larsen, Y. Huang, J. A. Rogers, *Nat. Commun.* **2014**, *5*, 3266.
- [23] N. Dolatsha, M. Shahabadi, R. Dehbashi, *J. Electromagn. Waves Appl.* **2008**, *22*, 1599.
- [24] J. S. Ho, A. S. Y. Poon, *Prog. Electromagn. Res.* **2014**, *148*, 151.
- [25] J. S. Ho, A. S. Y. Poon, in *Proc. IEEE Int. Symp. on Antennas Propag.* **2016**, 881.